Photoreceptor Structure in *GNAT2*-Associated Achromatopsia

Michalis Georgiou,[1,2] Navjit Singh,[1,2] Thomas Kane,[1,2] Anthony G. Robson,[1,2] Angelos Kalitzeos,[1,2] Nashila Hirji,[1,2] Andrew R. Webster,[1,2] Alfredo Dubra,[4] Joseph Carroll,[3] and Michel Michaelides[1,2]

[1]UCL Institute of Ophthalmology, University College London, London, United Kingdom
[2]Moorfields Eye Hospital NHS Foundation Trust, London, United Kingdom
[3]Department of Ophthalmology & Visual Sciences, Medical College of Wisconsin, Milwaukee, Wisconsin, United States
[4]Department of Ophthalmology, Stanford University, Palo Alto, California, United States

Correspondence: Michel Michaelides, UCL Institute of Ophthalmology, 11-43 Bath Street, London, EC1V 9EL, UK; michel.michaelides@ucl.ac.uk.

Received: August 29, 2019
Accepted: December 14, 2019
Published: March 23, 2020

Citation: Georgiou M, Singh N, Kane T, et al. Photoreceptor structure in *GNAT2*-associated achromatopsia. *Invest Ophthalmol Vis Sci.* 2020;61(3):40. https://doi.org/10.1167/iovs.61.3.40

Purpose. The purpose of this study was to report *GNAT2*-associated achromatopsia (*GNAT2*-ACHM) natural history, characterize photoreceptor mosaic, and determine a therapeutic window for potential intervention.

Methods. Patients with *GNAT2*-ACHM were recruited from a single tertiary referral eye center (Moorfields Eye Hospital, London, UK). We performed longitudinal clinical evaluation and ophthalmic examination, and multimodal retinal imaging, including adaptive optics scanning light ophthalmoscopy, quantitative analysis of the cone mosaic, and outer nuclear layer (ONL) thickness, including cone densities evaluation in selected regions of interest and comparison with reported healthy controls.

Results. All nine subjects (3 women) presented with nystagmus, decreased visual acuity (VA), light sensitivity, and highly variable color vision loss. One patient had normal color vision and better VA. Mean VA was 1.01 (±0.10) logarithms of the minimal angle of resolution (LogMAR) at baseline, and 1.04 (±0.10) LogMAR after a mean follow-up (range) of 7.6 years (1.7–12.8 years). Optical coherence tomography showed preservation of the foveal ellipsoid zone (EZ; $n = 8$; 88.9%), and EZ disruption ($n = 1$; 11.1%). Mean ONL thickness (range, ± SD) was 84.72 µm (28.57–113.33, ± 25.46 µm) and 86.47 µm (28.57–113.33, ± 24.65 µm) for right and left eyes, respectively. Mean cone densities (±SD) at 190 µm, 350 µm, and 500 µm from the foveal center, were 48.4 (±24.6), 37.8 (±14.7), and 30.7 (±9.9), $\times 10^3$ cones/mm^2, respectively. Mean cone densities were lower than these of unaffected individuals, but with an overlap.

Conclusions. The cone mosaic in *GNAT2*-ACHM is relatively well preserved, potentially allowing for a wide therapeutic window for cone-directed interventions.

Keywords: adaptive optics, retinal phenotyping, inherited retinal diseases, genetics, *GNAT2*, achromatopsia

GNAT2 (ACHM4, OMIM139340) autosomal recessive variants can cause both complete achromatopsia (cACHM),[1,2] and incomplete achromatopsia (iACHM).[3,4] Patients with GNAT2-related achromatopsia (*GNAT2*-ACHM) exhibit nystagmus beginning at birth / early infancy, photophobia, abnormal color vision, and poor visual acuity (VA).[5] Color vision testing is usually abnormal, with no color discrimination observed in most patients[6–9]; although some patients may retain some color vision.[3,7] A study suggested that the retention of color vision may be related to variants that result in some functional protein product.[3]

Fundoscopy usually reveals a normal retinal appearance, although some patients exhibit an abnormal foveal reflex or atrophy.[7] Full-field ERG testing typically reveals absent/markedly reduced cone function, albeit variable between patients, along with preserved rod function. The rod-specific ERG components are typically normal, although the scotopic strong flash ERG a-waves may be mildly subnormal,[7] reflecting loss of dark adapted cone system contribution. Spectral domain optical coherence tomography (SD-OCT) usually reveals relatively well-maintained foveal architecture without hypoplasia, but may exhibit a hyporeflective zone at the fovea.[10,11] Longitudinal optical coherence tomography (OCT) assessment of *GNAT2*-ACHM has been reported in only four subjects, from a single pedigree, over a period of 2 years.[11]

Adaptive optics provides the opportunity of advanced retinal imaging for in-depth phenotyping in inherited retinal diseases, with cellular resolution of the photoreceptor mosaic.[12] Adaptive optics corrects for the eye's monochromatic aberrations.[13,14] A confocal detector enables visualization of cones based on their waveguiding ability.[15,16] The waveguiding ability is thought to require intact outer segments.[17] Early investigations with confocal adaptive optics scanning light ophthalmoscopy (AOSLO) identified increased cone spacing and decreased cone

density in patients with ACHM, although these cones appeared as "dark spaces."[18–21] Marked variability in the cone mosaic has been observed across patients; among the two most common genotypes, *CNGA3* and *CNGB3*.[10,19,22] In contrast, in *ATF6*-ACHM and *PDE6C*-ACHM, few if any residual foveal cones were identified.[23,24] The *GNAT2*-ACHM genotype is associated with the relatively least disrupted photoreceptor mosaic.[6,20] Simultaneous confocal and split-detection AOSLO has allowed the identification of cone inner segment structure in the previously described "dark spaces."[25–28] *GNAT2*-ACHM was only investigated with confocal AOSLO imaging in two pedigrees to date.[6,20]

CNGB3 and *CNGA3* are responsible for 70% of the reported ACHM cases and are the most well studied genotypes, with on-going gene therapy trials (ClinicalTrials.gov numbers: NCT03758404, NCT02935517 NCT03001310, NCT02599922, and NCT02610582). Three homologous mouse models *of GNAT2*-ACHM have been described to date.[29–31] In the *Gnat2*^{cpfl3} mouse model, gene supplementation was observed to improve cone-mediated ERGs and restoring visual acuity (optomotor behavior).[32] A recent study from Felden et al. estimated the prevalence of *GNAT2*-ACHM to be 1.7%, in a cohort of 1116 independent ACHM families.[8] Due to its low prevalence, a limited number of studies have focused on phenotyping *GNAT2*-ACHM, despite the advancements in the field of gene therapy.

As cone photoreceptors are the target for gene replacement therapies in ACHM, it is important to assess how the cones are affected by *GNAT2* sequence variants, to thereby better understand the potential for future functional rescue. In this study, subjects with disease-causing sequence variants in *GNAT2* underwent detailed longitudinal phenotyping.

Methods and Materials

This study was approved by the Ethics Committee of Moorfields Eye Hospital. Written informed consent was obtained from all subjects attending research appointments after explanation of the nature and possible consequences of the study. The research followed the tenets of the Declaration of Helsinki.

Subjects

Nine subjects (3 women; 33%) from four pedigrees, with likely disease-causing sequence variants in *GNAT2*, were identified in the genetics database of Moorfields Eye Hospital, London, UK. All subjects were invited for a research appointment, including AOSLO imaging. Six subjects were recruited and attended a detailed research visit, and all available data of all nine subjects were used for evaluating disease natural history. Five of the patients were previously published (Supplementary Table S1).

Genetics

All patients harbored previously reported *GNAT2* variants.[1,8,34] Two pedigrees harbor nonsense mutations, leading to premature termination of translation, one pedigree harbored a missense mutation, and one pedigree a 4-bp insertion leading to a frameshift. Demographics and genetics are summarized in Supplementary Table S1.

Ocular Examination

All patients are under the care of a medical retina and ocular genetics consultant (M.M. and A.R.W.) in a single tertiary referral center (Moorfields, Eye Hospital, London, UK). All available notes and clinical data are reviewed.

Spectral-Domain OCT

SD-OCT imaging was performed in both eyes, following cycloplegia and pupillary dilation with tropicamide 1% and phenylephrine 2.5% eye drops. Horizontal line and volume scans were acquired with the Spectralis device (Heidelberg Engineering, Heidelberg, Germany), using the same protocol as that used by Aboshiha et al.[11] To address challenges due to nystagmus, the device was used in follow-up mode, so that the same scanning location was imaged at follow-up and baseline, and if this was not possible, the method described by Tee *et al.* was used, to ensure serial analysis of the same subject-specific retinal location.[35] The outer nuclear layer (ONL) thickness was calculated as the distance between the internal limiting membrane and the external limiting membrane, using the longitudinal reflectivity profiles on ImageJ, as previously described by Langlo et al.[28] Qualitative assessment of foveal structure was performed by grading SD-OCT images into one of five categories, as previously reported by Sundaram et al.: (1) continuous ellipsoid zone (EZ), (2) EZ disruption, (3) EZ absence, (4) presence of a hyporeflective zone, or (5) outer retinal atrophy.[10] For each subject, both right and left eyes were graded at baseline and follow-up visits. The presence/absence of foveal hypoplasia was also noted, defined as the persistence of one or more inner retinal layers (outer plexiform layer, inner nuclear layer, inner plexiform layer, or ganglion cell layer) through the fovea.

AOSLO Imaging of the Photoreceptor Mosaic

High-resolution imaging was attempted in six subjects using a previously described custom-built AOSLO,[36] at Moorfields Eye Hospital/UCL Institute of Ophthalmology, London, UK. Imaging with confocal and split-detection (non-confocal) was performed.

Pupil dilation and cycloplegia was achieved similarly to OCT imaging. Images were obtained over the central retina, and in strips extending from the fovea to 10 degrees in the temporal meridian, when time allowed. Image sequences were recorded as AVI files, of 150 frames, either at 1° or/and 1.5° square field of view. A desinusoiding algorithm was applied to each image sequence and individual frames were selected,[37] registered,[38] and averaged, to increase signal-to-noise ratio, for subsequent analysis. The final images were combined into a single montage (Adobe Photoshop, Adobe Systems Inc., San Jose, CA, USA) in layers for the different detection schemes using a custom-built automated software.[39] The scale was determined first in degrees per pixel in an image of a Ronchi ruling of known spacing after each imaging session. Then, the value was linearly scaled using the subject's axial length. Axial length was measured using the Zeiss IOL Master (IOL Master; Carl Zeiss Meditec, Dublin, CA, USA).

Cone densities were used for quantitative assessment of AOSLO imaging, as previously described.[40] The foveal center was too dense in all subjects to be analyzed, with

the location of the foveal center defined as the center of the nonanalyzable area (crossing point of maximum height and width). Eighty-five microns square regions of interest (ROIs) were marked in the cone mosaic at regular intervals from the foveal center in the temporal meridian. The distances measured from the center of the ROIs to the foveal center were: 190 µm (R1), 350 µm (R2), 500 µm (R3), 900 µm (R4), 1500 µm (R5), 2000 µm (R6), and 2500 µm (R7). ROIs R4 to R7 were available only for one subject. The R1 ROIs were cropped and imported into a semi-automated custom software for cone counting by a single experienced grader (M.G.). Automated cone identification was achieved by the software, finding local maxima in image brightness, based on previously described algorithms for R1 to R3 confocal images.[41,42] The grader was able to automatically remove identified cones or manually add cones, and could adjust the brightness and contrast of the confocal image on both linear and log scale. For R4 to R7, split-detection imaging was used for manual cone counting with the software due to the ambiguity between rod and cone photoreceptors present in confocal imaging. Bound cone density was then calculated by dividing the total number of bound Voronoi cells in an ROI by the total bound Voronoi area within the ROI, as previously described.[40,43] The aforementioned approach, with the exception of use of split-detection, is similar to the recently reported study in the literature by Jackson et al.,[40] in order to compare with their normative data acquired with a similar AOSLO system.

Color Vision Testing

Hardy-Rand-Rittler pseudoisochromatic plates (AO-HRR, 4th edition; Richmond Products, Inc., Albuquerque, NM, USA) were presented under a Daylight Illuminator (Richmond Products, Inc.) and scored using the accompanying worksheet.

A commercially available low vision version of the Cambridge Colour Test (lvvCCT) trivector version was performed using the Metropsis system (Cambridge Research Systems Ltd., Rochester, Kent, UK). The test stimuli were presented on a calibrated 32-inch monitor, with a refresh rate of 120 Hz, 1920 × 1080 pixels spatial resolution, and up to 16-bit (per channel) color resolution. The stimuli consisted of four homogeneous discs presented simultaneously on a 2-cd/m^2 neutral background in a diamond-shaped array. Each disc subtended 4 degrees, and was separated by 2.5 degrees from the adjacent discs. The viewing distance was 150 cm. On each presentation, one of the discs differed in chromaticity from the remaining three, which remained of neutral hue. The patient was instructed to report which of the four discs was different in color,[44] by pressing the corresponding key on a five-key RB-540 Cedrus response box (Cedrus, San Pedro, CA, USA). Color discrimination was probed along the Protan, Deutan, and Tritan confusion axes. For each axis, the corresponding saturation of the color disc would decrease or increase according to whether the patient answered correctly or incorrectly to the previous trial, respectively. On completion of the test, the lvvCCT returned the saturation threshold along each confusion axis, which represents the minimum saturation required to discriminate the color disc from the achromatic discs. Both color vision tests were performed monocularly.

Statistical Methods

Statistical analysis was performed with IBM SPSS Statistics for Windows (version 22.0; IBM Corp., Armonk, NY, USA).

Results

Clinical Presentation

All subjects presented with nystagmus, decreased VA, light sensitivity, and highly variable color vision loss. The fundus appearance was unchanged over time with abnormal foveal reflex, but without any evidence of frank atrophy or pigmentation. Only in one patient (P6), subtle foveal changes were observed, without evidence of progression. Fundoscopy findings were documented in six patients with color fundus photography (Supplementary Fig. S1).

Color vision testing was reported in detail by Michaelides et al. for subjects P6 to P9, with evidence of some residual color discrimination in three of the four patients (P6, P8, and P9).[7] Patients P1, P2, and P3 showed no residual color discrimination on testing with HRR pseudoisochromatic plates. Interestingly, patient P4 was able to name colors and correctly identified all the pseudoisochromatic plates. On further testing with lvvCCT trivector version,[44,45] color discrimination was probed along the Protan, Deutan, and Tritan confusion axes, with nearly normal saturation thresholds, thereby suggesting no color deficit.

Longitudinal VA data were available for all patients (mean age at baseline [range], 26.3 [6.4−48.9] years old, and mean follow-up [range],: 7.6 years [1.7−12.8 years]). Patient P4, with normal color discrimination, also had the best VA in the cohort; 0.60 LogMAR at baseline and stable at 0.61 LogMAR after 8 years of follow-up. Mean VA (±SD) for both eyes at baseline was 1.01 LogMAR (±0.05), ranging from 0.90 LogMAR to 1.10 LogMAR, and at follow-up it was 1.04 LogMAR (±0.10), ranging from 0.90 LogMAR to 1.36 LogMAR for the rest of the subjects. Patient P5 had all assessments and analyses done monocularly due to congenital cataract and amblyopia in the right eye, complicated later in life with subretinal exudates similar to Coats' disease, leading to exudative retinal detachment, and hand movement vision. For the rest of the cohort, best-corrected VA was similar between eyes both at baseline ($P = 0.921$;, $t = 0.103$, and $df = 7$) and follow-up (P=0.608, $t = 0.537$, and $df = 7$). VA was stable over time ($P = 0.399$, $t = 0.899$, and $df = 7$), over a mean follow-up of 7.5 years (range, 1.7−12.8). All patients reported stable vision, with no new visual complaints over time. The spherical equivalent varies greatly among subjects from -10.0 D to +5.75 D.

Retinal Morphology: SD-OCT

Mean age ± SD at baseline OCT was 28.6 ± 15.4 years, mean follow-up time (range) was 4.9 years (1.7−10.5 years). Eight patients had a continuous EZ (grade 1; Fig. 1) and one patient (P6) had a hyporeflective zone at the fovea (grade 4; Fig. 3). Mean ONL thickness (range, ± SD) was 84.72 µm (28.57−113.33, ± 25.46 µm) and 86.47 µm (28.57−113.33, ± 24.65 µm) for the right and left eyes, respectively. The ONL thickness was similar between eyes ($P = 0.903$, $t = 0.126$, and $df = 8$; Fig. 2A). The mean baseline ONL thickness for right eyes did not correlate with subject age ($P = 0.744$, $r = -0.127$, Pearson correlation; Fig. 2B).

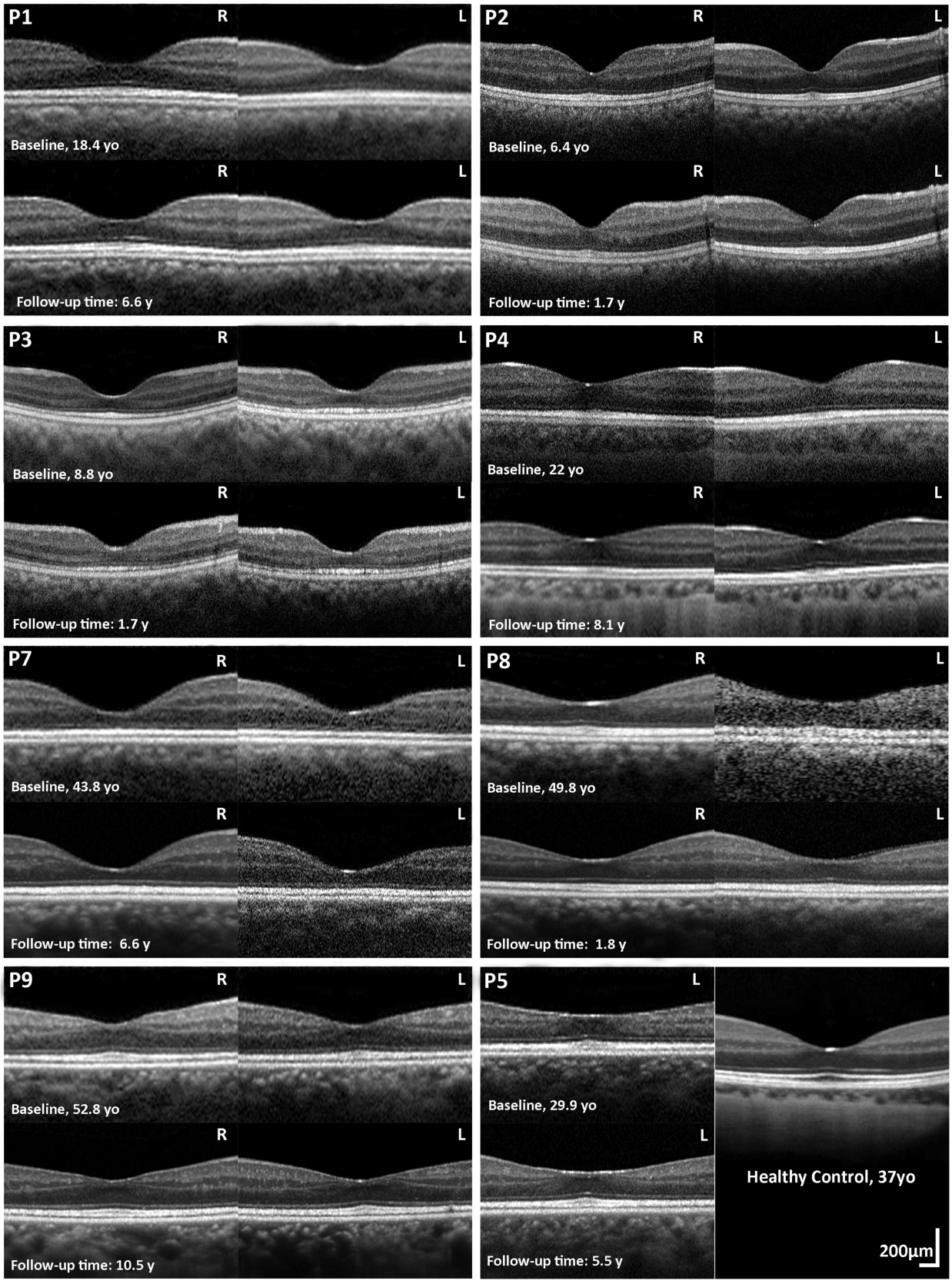

Figure 1. Spectral domain optical coherence tomography (SD-OCT) in cases with continuous ellipsoid zone (EZ). Longitudinal transfoveal OCT line scans for both eyes are presented for patients P1, P2, P3, P4, P7, and P9. Patient P5 had imaging data only for the left eye. For the

Investigative Ophthalmology & Visual Science

young siblings, patients P2 and P3, vertical scans are presented; because horizontal transfoveal scans could not be obtained due to strong nystagmus. For the rest of the patients, scans are horizontally orientated to the fovea. No evidence of progression was present in any of the patients. EZ appears continuous and thickened with increased reflectivity. A transfoveal OCT scan of a healthy subject is provided for comparison. R, right eye; L, left eye; yo, years old; y, years.

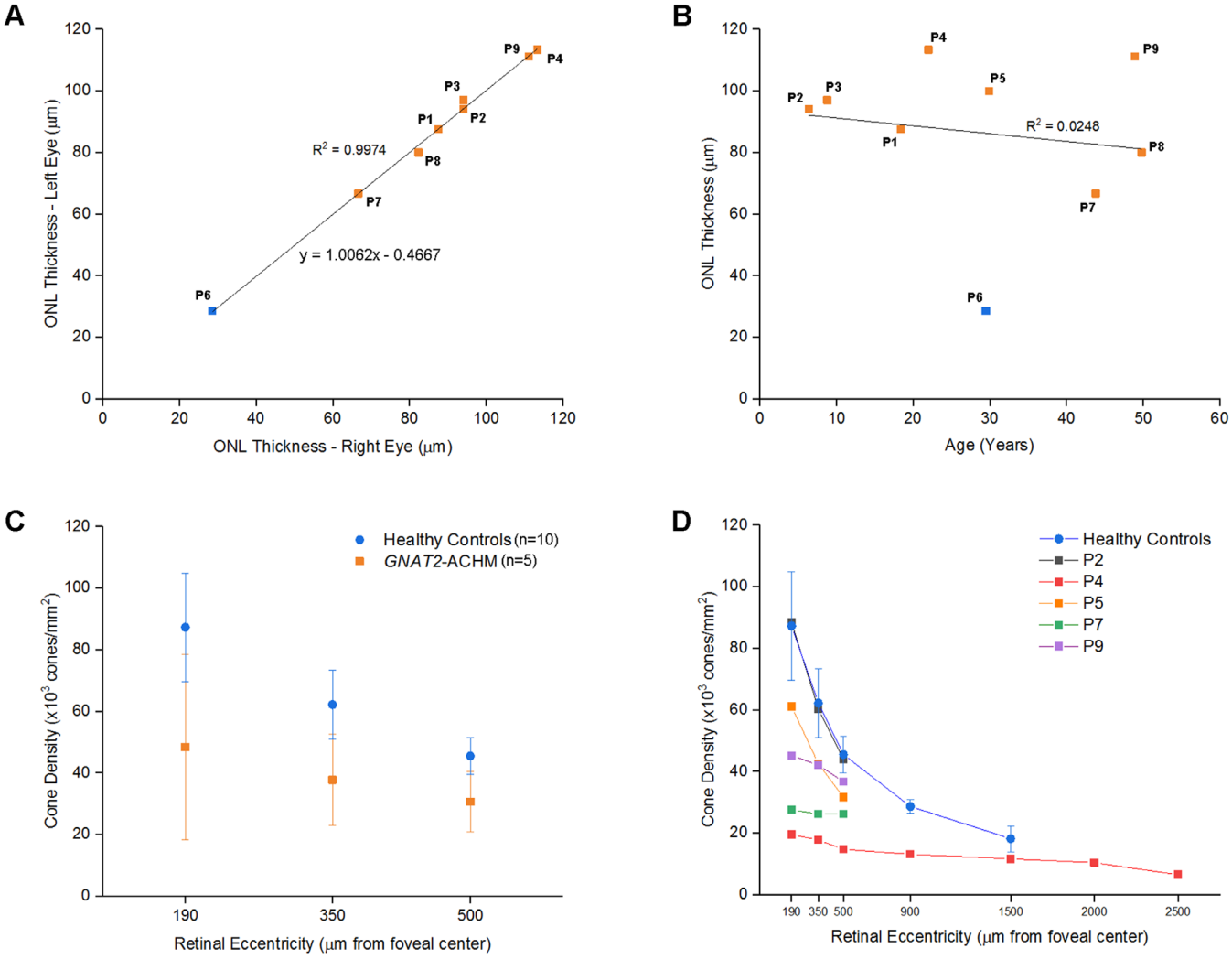

Figure 2. Quantitative imaging analysis graphs. (**A**) High interocular agreement was observed between the outer nuclear layer (ONL) thicknesses between eyes. (**B**) The ONL thickness is not correlated with age. ONL thicknesses for the left eyes are presented, because the left eye was only available for patient P5. The blue score on **A** and **B** represents patient P6; the only patient in the cohort with disrupted foveal ellipsoid zone. Previously reported mean (± SD) foveal ONL thickness for subjects with *CNGB3*- and *CNGA3*-ACHM was 79.2 ± 18.7 µm and 112.1 ± 13.9 µm for healthy controls.[47] (**C**) Mean (± SD) cone densities per eccentricity for patients with *GNAT2* of our cohort and healthy controls reported by Jackson et al.[40] Cone densities were lower, on average, for subjects with *GNAT2* compared to healthy controls in all three parafoveal eccentricities (190 µm, 350 µm, and 500 µm), but a small overlap was observed. (**D**) Cone densities per eccentricity of all individuals and mean of healthy controls. Patient P4, with the best visual acuity and normal color vision, had the lowest cone densities at all eccentricities. Patient P2, the youngest patient in the cohort, had cone densities similar to the average cone densities for healthy controls. Patients P7 and P9, the oldest in the cohort, showed lower cone densities.

At follow-up visits, mean ONL thickness (range, ± SD) was 85.99 µm (28.57–113.33, ± 25.46 µm) and 86.67 µm (28.57–123.08, ± 26.15 µm) for the right and left eyes, respectively. No change was observed throughout follow-up, without any evidence of progression in any of the patients (Figs. 1, 3). ONL thickness (mean ± SD) of 105 ± 12.2 µm (mean age ± SD; 29 ± 8 years) has previously been reported in unaffected controls ($n = 93$).[46] There is overlap between this normative data and our cohort, both at baseline and follow-up. For *CNGA3*- and *CNGB3*-ACHM ONL thickness (mean ±SD) of 79.2 ± 18.7 µm (mean age ± SD; 24 ± 14 years) has previously been reported.[47] Of note, patient P6 has significant ONL thinning compared to the rest of the cohort (Figs. 2A,B, Fig. 3), and outside of the limits of the normative data. No foveal hypoplasia was observed in any of the patients (Figs. 1, 3). OCT and additional FAF findings are summarized in Supplementary Table S2 and Supplementary Figure S2.

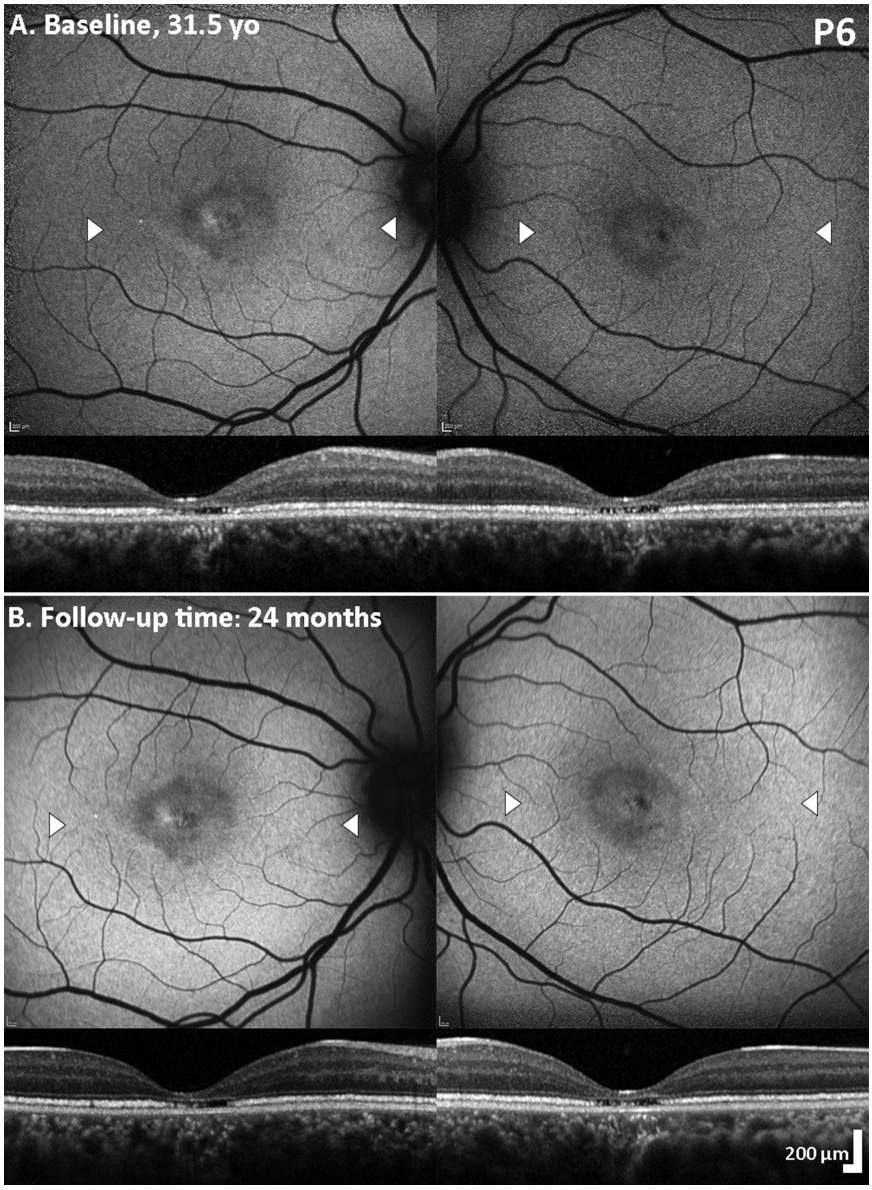

Figure 3. Spectral domain optical coherence tomography (SD-OCT) and fundus autofluorescence (FAF) Imaging in the patient with foveal photoreceptor disruption. FAF and corresponding transfoveal horizontal OCT scans of both eyes at baseline (**A**) and 2 years follow-up (**B**). Focal foveal mottling with increased/decreased autofluorescence signal is observed without evidence of progression. White arrow heads mark the border of the OCT line scan presented below each corresponding FAF image; with prominent foveal thinning and foveal disruption of the ellipsoid zone (EZ) in both eyes. Beyond the foveal center, the EZ was thickened and hyper-reflective, in keeping with the rest of the cohort, and without any progression between visits. yo, years old.

Photoreceptor Mosaic Assessed with AOSLO Imaging

Six subjects underwent AOSLO imaging (patients P2–P5, P7, and P9). Axial length was measured for those subjects and was used to scale the final photoreceptor mosaic. Mean axial length for right and left eyes (range, ± SD) was 24.18 (±2.54, 21.64–29.23) mm and 24.15 (±2.55, 21.70–29.27) mm, respectively. Mean age (range, ± SD) for the *GNAT2* subjects with analyzable AOSLO images was 35 (±17, 8–59) years and for the previously reported healthy controls was 28 (±11, 18–54) years.[40] Patient P4 (normal color vision) and patients P5, P7, and P9 were successfully imaged, and the photoreceptor mosaic was available for quantitative analysis (Fig. 4). Siblings P2 to P3 were the most challenging to image due to their young age (8.1 and 10.5 years old), and strong nystagmus, not only for AOSLO, but also for OCT, albeit to a lesser extent for the latter. Analyzable high quality images were achieved only from sibling P2; however, the exact location of those images was difficult to identify because the final montage was not centered on the fovea, and due to a lack of major anatomic landmarks (e.g., blood vessels) that could allow alignment with other imaging modalities. We tried to analyze ROIs maintaining the same distances as the rest of the cohort measuring from the center of the denser area of the mosaic. Cone densities at the ROIs for patient P2 were the highest in the cohort and match those from unaffected individuals for a given eccentricity

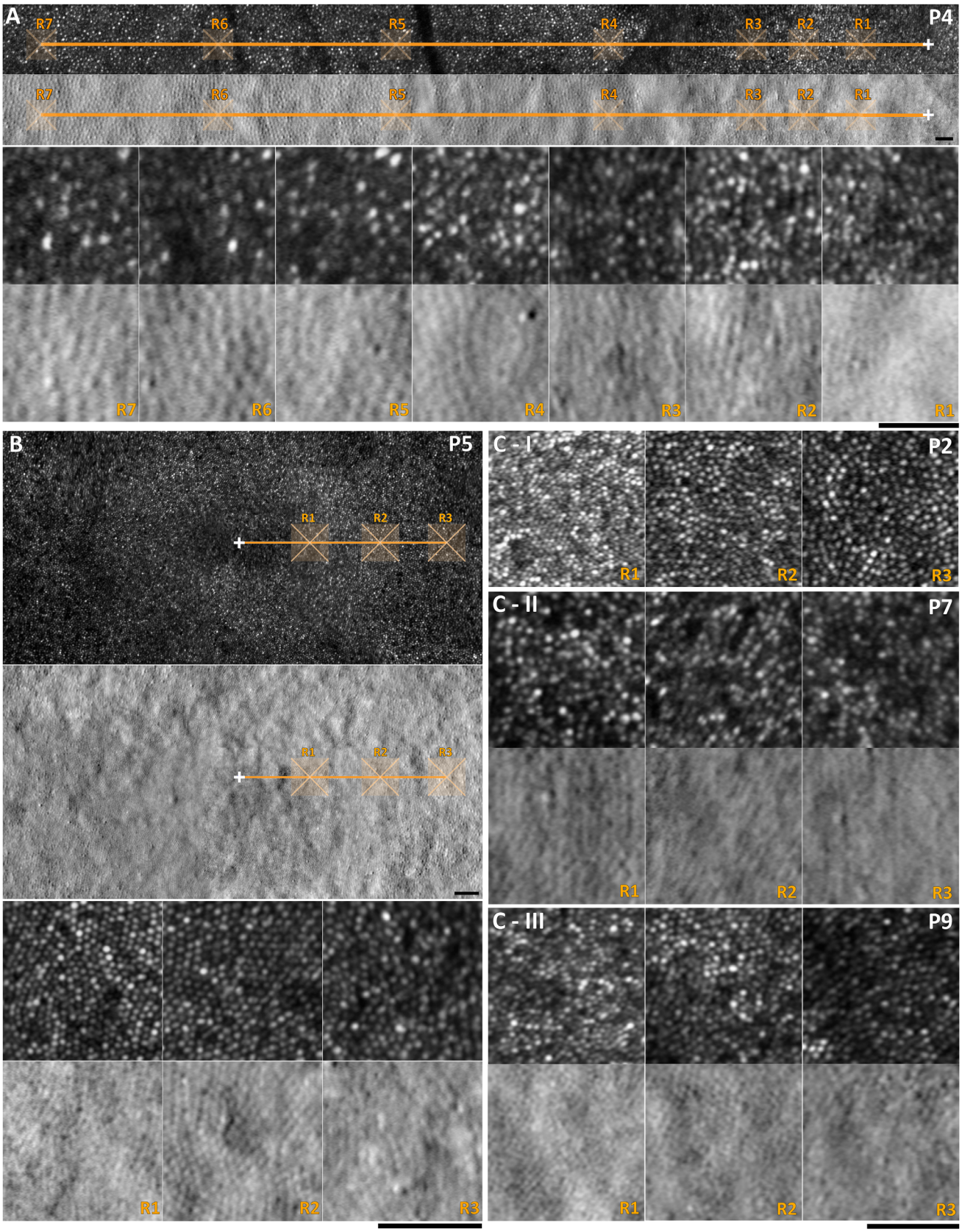

Figure 4. Adaptive optics scanning light ophthalmoscopy (AOSLO) imaging in *GNAT2*-ACHM. The white cross marks the foveal center and the orange line the temporal meridian. The regions of interest (ROIs) are marked with semi-transparent orange 85 µm squares. (**A**) Patient P4 has extensive imaging data up to 2500 µm (R7) temporally to the foveal center. First row: Confocal AOSLO image with marked ROIs shown in the third row in greater magnification. Second row: Co-localized split-detection image, with marked ROIs shown on the fourth row. For R1 to R3, cone counting was done using confocal detection. For R4 to R7, split-detection was more informative of the cone mosaic

Investigative Ophthalmology & Visual Science

due to interference of rods on confocal imaging. (**B**) Foveal photoreceptor mosaic of the left eye of patient P5. Top: Confocal AOSLO image with ROIs presented in higher magnification on the third row. Second row: Split-detection image with ROIs presented on the fourth row. The mosaic was regularly organized and cone densities were at the lower limit of the normal range. (**C**) ROIs for patients P2, P7, and P9 (R1: 190 µm, R2: 350 µm, and R3: 500 µm). (**C-I**) Patient P2 is the youngest patient of the cohort and had cone densities similar to the average cone densities in unaffected individuals. Due to the high density, split-detection imaging was not informative at those locations, hence is not shown. (**C-II, III**) Patients P7 and P9 are the oldest in the cohort and have a sparser mosaic. Scale bars = 50 µm.

Table. Cone Density Measurements

	Cone Density ($\times 10^3$ cones/mm^2)						
Patient*	**R1‡ (190 µm)**	**R2 (350 µm)**	**R3 (500 µm)**	**R4 (900 µm)**	**R5 (1500 µm)**	**R6 (2000 µm)**	**R7 (2500 µm)**
P2	88.4	60.3	44.0	NA	NA	NA	NA
P4	19.6	17.8	14.8	13.2	11.1	10.4	6.5
P5	61.1	42.4	31.7	NA	NA	NA	NA
P7	27.6	26.2	26.2	NA	NA	NA	NA
P9	45.2	42.1	36.8	NA	NA	NA	NA
Mean for the cohort (± SD)	48.4 (±24.6)	37.8 (±14.7)	30.7 (±9.9)	NA	NA	NA	NA
Normative Data† (± SD)	87.3 (±17.6)	62.2 (±11.2)	45.5 (±6.0)	28.7 (±6.0)	18.2 (±4.2)	NA	NA

Additional information (sex, age, spherical equivalent, visual acuity) are presented In Supplementary Table S3.
* All patients have normal fundus autofluorescence appearance and intact ellipsoid zone on OCT.
‡ Regions of interest (R1 to R7; distance from foveal center).
† From Reference 40.

(Fig. 2D, Figs. 4C–**I**). Analyzable ROIs for 190 µm (R1), 350 µm (R2), and 500 µm (R3) away from the fovea were available for all 5 patients (Fig. 4). For subject P4, data out to 2500 µm temporal to the foveal center were available (Fig. 4A). Cone densities for all ROIs and mean cone densities per eccentricity are presented in the Table and plotted in Figures 2C,D.

Discussion

In this study, we assessed photoreceptor structure in a series of patients with the ultra-rare form of *GNAT2*-associated ACHM, including cross-sectional and longitudinal analyses of structural and functional features. The findings indicate that *GNAT2*-retinopathy has distinct features that differ from other forms of ACHM, with a dissociation between the observed photoreceptor mosaic and function, relevant to potential future therapeutic gene supplementation interventions.

Foveal hypoplasia is a common feature in ACHM cohorts: all reported subjects with *ATF6*-ACHM,[23] and two thirds of the reported *CNGA3*- and *CNGB3*-ACHM subjects, have foveal hypoplasia.[10,22,28] In our cohort of *GNAT2*-ACHM, no case of foveal hypoplasia was observed, a finding similar to *PDE6C*-ACHM.[24] *GNAT2* encodes guanine nucleotide-binding protein G(t) subunit alpha-2, which is part of the transducin complex, a G-protein participating in the visual cycle.[48,49] The α-subunit is released from $\beta\gamma$ subunits after the interaction with light activated photopigment in cone cells and the exchange of GDP for GTP. The released α-subunit activates the cGMP phosphodiesterase (PDE6C), which lowers the cGMP and hyperpolarizes photoreceptors.[50] Interestingly, despite both molecules being involved in a sequential path in the phototransduction cascade and both causing ACHM, *PDE6C*-ACHM presents with far more severe structural defects than *GNAT2*-ACHM.[24] Structural integrity of the EZ on OCT was evident in all *GNAT2* subjects (Fig. 1), with the exception of subject P6 (Fig. 3) - representing an example of the structural intrafamilial variability commonplace in inherited retinal diseases.[49] The other four affected individuals from the same pedigree showed a continuous EZ, with three of the subjects being older. Functional intrafamilial variability has also been reported in the same pedigree.[7] Similar structural intrafamilial variability has also been reported in pedigrees of *CNGA3*-ACHM.[22] Due to the recessive inheritance and the rarity of ACHM, data for intrafamilial variability are limited. The above finding of loss of foveal EZ in patient P6, combined with the stable imaging findings over follow-up (Fig. 3), supports the notion that major EZ loss is an event during early childhood,[51] rather than a progressive phenomenon later in life.[52] In the ongoing debate about the stationary or progressive nature of ACHM, different genotypes should be studied individually. *PDE6C*-ACHM was recently reported as a slowly progressive maculopathy.[24] ACHM studies with different proportions of patients with *GNAT2* and *PDE6C* have shown conflicting results.[52,53] Thiadens et al., in a cohort with five patients with *PDE6C* (20%) and no *GNAT2*, concluded that ACHM was often a progressive disease.[53] Hirji et al., in a cohort with one subject with *PDE6C* (2%) and two subjects with *GNAT2* (4%), concluded that ACHM was predominantly stationary.[52]

In the current study we extend the phenotypic spectrum of *GNAT2*-retinopathy. Patient P4 had color vision, the best acuity among this cohort (albeit decreased) and the thickest foveal ONL, despite low parafoveal cone densities. The milder phenotype can be attributed to the homozygous missense variant, which may translate into a protein product with residual function, in contrast to the rest of the cohort harboring null variants (Supplementary Table S1). Felden et al. in their genotyping study, reported a patient (CHRO768-II:1) with the same homozygous variant, without, however, any color vision or ERG data available.[8] Interestingly, this patient had undetectable standard light-adapted (LA30Hz; LA3) ERGs, when tested with International-standard full-field ERGs,[54] and undetectable pattern ERG.[55]

The recording to short wavelength flashes on an amber background (S-cone ERG; stimulus duration 5 ms)[56] was simplified and subnormal bilaterally (Supplementary Fig. S3). The observed color vision in our patient was better than previously reported residual color vision in *GNAT2*,[3,6,8] including the previously reported pedigree included in our study.[7] Despite the milder phenotype observed in patient P4, cone densities at all ROIs were the lowest in the cohort (Fig. 2D), that might suggest a different disease mechanism than the rest of the subjects, with cones with residual function but decreased in number.

There was an overlap between the range of cone densities in our cohort and healthy controls, in all three locations near the fovea (R1−R3),[40] with greater variability observed in subjects with *GNAT2* (Fig. 2C, Table). The youngest patient of the cohort had the best-preserved mosaic and the highest densities (Figs. 4,C−I). However, with increasing age, there was a trend for lower densities. In all subjects, EZ was continuous on OCT (Fig. 1). The focal disruptions or increased spacing of the mosaic, leading to lower cone densities, were easier to identify with AOSLO compared to OCT (Fig. 1). Peak cone density could not be estimated in any of the subjects with *GNAT2* due to the unresolvable, densely packed mosaic at the foveal center. In contrast, in *CNGA3*- and *CNGB3*-ACHM, peak cone density is severely reduced, with mean densities lower than the reported values for R1 (190 µm away from the fovea) in our cohort.[22,28] Scotoma on mesopic microperimetry was reported in all examined patients with *GNAT2* (4/4), whereas only in 1 of 33 subjects examined with *CNGA3*- and *CNGB3*-ACHM.[10] In addition, BCVA, contrast sensitivity, reading acuity, and mean sensitivity were lower in the *GNAT2* compared with the *CNGA3* or *CNGB3* groups.[10] The structure and reflectivity of the photoreceptor mosaic is better preserved in patients with *GNAT2*-ACHM compared to other ACHM genotypes.[20] In contrast to this disconnect, recent studies have shown cone spacing evaluated with AOSLO may correlate with functional assessments in patients with other inherited retinal degenerations, albeit with functioning photoreceptors.[57,58] This emphasizes the potential efficacy of gene replacement therapeutic intervention in subjects with *GNAT2*.

Limitations

AOSLO insights into disease progression are of great value, including identification of the optimal therapeutic window and participant stratification. In the current study, *GNAT2* subjects had cross-sectional AOSLO assessment. Longitudinal studies will be in a better position to evaluate evidence of progression. In addition, the functional and anatomic dissociation may be further investigated with scotopic testing using chromatic ERG full-field stimulus threshold, cone and rod specific microperimetry assessment protocols, and the evolving AOSLO-guided retinal sensitivity assessments ("nanoperimetry").[59–61]

Conclusions

This is the first in-depth analysis and longitudinal study of photoreceptor structure in *GNAT2*-associated ACHM. The data presented herein describe a potentially greater therapeutic window, compared to all other forms of ACHM reported to date (*CNGA3*, *CNGB3*, *PDE6C*, and *ATF6*). AOSLO imaging allows for a more sensitive assessment of the photoreceptor mosaic than OCT, despite the lower successful acquisition rate. Any age-dependent changes are subtle, with relative preservation of the cone mosaic observed until late adulthood.

Acknowledgments

Supported by grants from the National Institute for Health Research Biomedical Research Centre at Moorfields Eye Hospital National Health Service Foundation Trust and UCL Institute of Ophthalmology, Retina UK, Onassis Foundation, Leventis Foundation, Moorfields Eye Hospital Special Trustees, and Moorfields Eye Charity (R180004A), The Wellcome Trust (099173/Z/12/Z), Research to Prevent Blindness Departmental Challenge Award (Stanford), and the Foundation Fighting Blindness (USA). Research reported in this publication was supported in part by the National Eye Institute of the National Institutes of Health under Award Number R01 EY017607, P30 EY026877, U01 EY025477, R01 EY028287, and R01 EY025231. The content is solely the responsibility of the authors and does not necessarily represent the official views of the National Institutes of Health.

MG drafted the manuscript. MG, NS, TK, NH, ARG, and AK collected and analyzed data. MM, ARW, AD, and JC conceived, supervised, and revised the manuscript. All authors provided critical revision of the manuscript.

Disclosure: **M. Georgiou,** None; **N. Singh,** None; **T. Kane,** None; **A.G. Robson,** None; **A. Kalitzeos,** None; **N. Hirji,** None; **A.R. Webster,** None; **A. Dubra,** None; **J. Carroll,** MeiraGTx (F, C), Applied Genetic Technologies Corporation (F), and Optovue Inc. (F), Translational Imaging Innovations (I); **M. Michaelides,** MeiraGTx (C)

References

1. Aligianis IA, Forshew T, Johnson S, et al. Mapping of a novel locus for achromatopsia (ACHM4) to 1p and identification of a germline mutation in the alpha subunit of cone transducin (*GNAT2*). *J Med Genet*. 2002;39:656–660.
2. Kohl S, Baumann B, Rosenberg T, et al. Mutations in the cone photoreceptor G-protein alpha-subunit gene GNAT2 in patients with achromatopsia. *Am J Hum Genet*. 2002;71:422–425.
3. Rosenberg T, Baumann B, Kohl S, et al. Variant phenotypes of incomplete achromatopsia in two cousins with GNAT2 gene mutations. *Invest Ophthalmol Vis Sci*. 2004;45:4256–4262.
4. Stockman A, Henning GB, Moore AT, et al. Visual consequences of molecular changes in the guanylate cyclase-activating protein. *Invest Ophthalmol Vis Sci*. 2014;55:1930–1940.
5. Hirji N, Aboshiha J, Georgiou M, et al. Achromatopsia: clinical features, molecular genetics, animal models and therapeutic options. *Ophthalmic Genet*. 2018;39:149–157.
6. Ueno S, Nakanishi A, Kominami T, et al. In vivo imaging of a cone mosaic in a patient with achromatopsia associated with a GNAT2 variant. *Jpn J Ophthalmol*. 2017;61:92–98.
7. Michaelides M, Aligianis IA, Holder GE, et al. Cone dystrophy phenotype associated with a frameshift mutation (M280fsX291) in the alpha-subunit of cone specific transducin (*GNAT2*). *Br J Ophthalmol*. 2003;87:1317–1320.
8. Felden J, Baumann B, Ali M, et al. Mutation spectrum and clinical investigation of achromatopsia patients with mutations in the GNAT2 gene. *Hum Mutat*. 2019; 40:1145–1155.

9. Ouechtati F, Merdassi A, Bouyacoub Y, et al. Clinical and genetic investigation of a large Tunisian family with complete achromatopsia: identification of a new nonsense mutation in GNAT2 gene. *J Hum Genet*. 2011;56:22–28.
10. Sundaram V, Wilde C, Aboshiha J, et al. Retinal structure and function in achromatopsia: Implications for gene therapy. *Ophthalmology*. 2014;121:234–245.
11. Aboshiha J, Dubis AM, Cowing J, et al. A prospective longitudinal study of retinal structure and function in achromatopsia. *Invest Ophthalmol Vis Sci*. 2014;55:5733–5743.
12. Georgiou M, Kalitzeos A, Patterson EJ, et al. Adaptive optics imaging of inherited retinal diseases. *Br J Ophthalmol*. 2018;102:1028–1035.
13. Rossi EA, Chung M, Dubra A, et al. Imaging retinal mosaics in the living eye. *Eye (Lond)*. 2011;25:301–308.
14. Liang J, Williams DR, Miller DT. Supernormal vision and high-resolution retinal imaging through adaptive optics. *J Opt Soc Am A Opt Image Sci Vis*. 1997;14:2884–2892.
15. Dubra A, Sulai Y, Norris JL, et al. Noninvasive imaging of the human rod photoreceptor mosaic using a confocal adaptive optics scanning ophthalmoscope. *Biomed Opt Express*. 2011;2:1864–1876.
16. Roorda A, Duncan JL. Adaptive optics ophthalmoscopy. *Annu Rev Vis Sci*. 2015;1:19–50.
17. Roorda A, Williams DR. Optical fiber properties of individual human cones. *J Vis*. 2002;2:404–412.
18. Carroll J, Choi SS, Williams DR. In vivo imaging of the photoreceptor mosaic of a rod monochromat. *Vision Res*. 2008;48:2564–2568.
19. Genead MA, Fishman GA, Rha J, et al. Photoreceptor structure and function in patients with congenital achromatopsia. *Invest Ophthalmol Vis Sci*. 2011;52:7298–7308.
20. Dubis AM, Cooper RF, Aboshiha J, et al. Genotype-dependent variability in residual cone structure in achromatopsia: Toward developing metrics for assessing cone health. *Invest Ophthalmol Vis Sci*. 2014;55:7303–7311.
21. Merino D, Duncan JL, Tiruveedhula P, Roorda A. Observation of cone and rod photoreceptors in normal subjects and patients using a new generation adaptive optics scanning laser ophthalmoscope. *Biomed Opt Express*. 2011;2:2189–2201.
22. Georgiou M, Litts KM, Kalitzeos A, et al. Adaptive optics retinal imaging in *CNGA3*-associated achromatopsia: Retinal characterization, interocular symmetry, and intrafamilial variability. *Invest Ophthalmol Vis Sci*. 2019;60:383–396.
23. Mastey RR, Georgiou M, Langlo CS, et al. Characterization of retinal structure in *ATF6*-associated achromatopsia. *Invest Ophthalmol Vis Sci*. 2019;60:2631–2640.
24. Georgiou M, Robson AG, Singh N, et al. Deep Phenotyping of *PDE6C*-Associated Achromatopsia. *Invest Ophthalmol Vis Sci*. 2019;60(15):5112–5123.
25. Scoles D, Sulai YN, Langlo CS, et al. In vivo imaging of human cone photoreceptor inner segments. *Invest Ophthalmol Vis Sci*. 2014;55:4244–4251.
26. Abozaid MA, Langlo CS, Dubis AM, et al. Reliability and repeatability of cone density measurements in patients with congenital achromatopsia. *Adv Exp Med Biol*. 2016;854:277–283.
27. Langlo CS, Erker LR, Parker M, et al. Repeatability and longitudinal assessment of foveal cone structure in CNGB3-associated achromatopsia. *Retina*. 2017;37:1956–1966.
28. Langlo CS, Patterson EJ, Higgins BP, et al. Residual foveal cone structure in *CNGB3*-associated achromatopsia. *Invest Ophthalmol Vis Sci*. 2016;57:3984–3995.
29. Ronning KE, Allina GP, Miller EB, et al. Loss of cone function without degeneration in a novel Gnat2 knock-out mouse. *Exp Eye Res*. 2018;171:111–118.
30. Jobling AI, Vessey KA, Waugh M, et al. A naturally occurring mouse model of achromatopsia: characterization of the mutation in cone transducin and subsequent retinal phenotype. *Invest Ophthalmol Vis Sci*. 2013;54:3350–3359.
31. Chang B, Dacey MS, Hawes NL, et al. Cone photoreceptor function loss-3, a novel mouse model of achromatopsia due to a mutation in Gnat2. *Invest Ophthalmol Vis Sci*. 2006;47:5017–5021.
32. Alexander JJ, Umino Y, Everhart D, et al. Restoration of cone vision in a mouse model of achromatopsia. *Nat Med*. 2007;13:685–687.
33. Weisschuh N, Stingl K, Audo I, et al. Mutations in the gene PDE6C encoding the catalytic subunit of the cone photoreceptor phosphodiesterase in patients with achromatopsia. *Hum Mutat*. 2018;39:1366−1371.
34. Carss KJ, Arno G, Erwood M, et al. Comprehensive rare variant analysis via whole-genome sequencing to determine the molecular pathology of inherited retinal disease. *Am J Hum Genet*. 2017;100:75–90.
35. Tee JJL, Carroll J, Webster AR, Michaelides M. Quantitative analysis of retinal structure using spectral-domain optical coherence tomography in RPGR-associated retinopathy. *Am J Ophthalmol*. 2017;178:18–26.
36. Dubra A, Sulai Y. Reflective afocal broadband adaptive optics scanning ophthalmoscope. *Biomed Opt Express*. 2011;2:1757–1768.
37. Salmon AE, Cooper RF, Langlo CS, et al. An automated reference frame selection (ARFS) algorithm for cone imaging with adaptive optics scanning light ophthalmoscopy. *Transl Vis Sci Technol*. 2017;6:9.
38. Dubra A, Harvey Z. Registration of 2D images from fast scanning ophthalmic instruments. Berlin, Heidelberg: Springer Berlin Heidelberg; WBIR 2010;6204.
39. Davidson B, Kalitzeos A, Carroll J, et al. Fast adaptive optics scanning light ophthalmoscope retinal montaging. *Biomedical Optics Express*. 2018;9:4317–4328.
40. Jackson K, Vergilio GK, Cooper RF, et al. A 2-year longitudinal study of normal cone photoreceptor density. *Invest Ophthalmol Vis Sci*. 2019;60:1420–1430.
41. Li KY, Roorda A. Automated identification of cone photoreceptors in adaptive optics retinal images. *J Opt Soc Am A Opt Image Sci Vis*. 2007;24:1358–1363.
42. Garrioch R, Langlo C, Dubis AM, et al. Repeatability of in vivo parafoveal cone density and spacing measurements. *Optom Vis Sci*. 2012;89:632–643.
43. Cooper RF, Wilk MA, Tarima S, Carroll J. Evaluating descriptive metrics of the human cone mosaic. *Invest Ophthalmol Vis Sci*. 2016;57:2992–3001.
44. Simunovic MP, Votruba M, Regan BC, Mollon JD. Colour discrimination ellipses in patients with dominant optic atrophy. *Vision Res*. 1998;38:3413–3419.
45. Kumaran N, Ripamonti C, Kalitzeos A, et al. Severe loss of Tritan color discrimination in RPE65 associated Leber congenital amaurosis. *Invest Ophthalmol Vis Sci*. 2018;59:85–93.
46. Carroll J, Dubra A, Gardner JC, et al. The effect of cone opsin mutations on retinal structure and the integrity of the photoreceptor mosaic. *Invest Ophthalmol Vis Sci*. 2012;53:8006–8015.
47. Mastey RR, Gaffney M, Litts KM, et al. Assessing the interocular symmetry of foveal outer nuclear layer thickness in achromatopsia. *Transl Vis Sci Technol*. 2019;8:21.
48. Lerea CL, Bunt-Milam AH, Hurley JB. Alpha transducin is present in blue-, green-, and red-sensitive cone photoreceptors in the human retina. *Neuron*. 1989;3:367–376.

Investigative Ophthalmology & Visual Science

49. Gill JS, Georgiou M, Kalitzeos A, et al. Progressive cone and cone-rod dystrophies: clinical features, molecular genetics and prospects for therapy. *Br J Ophthalmol*. 2018, 102(8):1028–1035.
50. Stryer L. Visual excitation and recovery. *J Biol Chem*. 1991;266:10711–10714.
51. Yang P, Michaels KV, Courtney RJ, et al. Retinal morphology of patients with achromatopsia during early childhood: implications for gene therapy. *JAMA Ophthalmol*. 2014;132:823–831.
52. Hirji N, Georgiou M, Kalitzeos A, et al. Longitudinal assessment of retinal structure in achromatopsia patients with long-term follow-up. *Invest Ophthalmol Vis Sci*. 2018;59:5735–5744.
53. Thiadens AA, Somervuo V, van den Born LI, et al. Progressive loss of cones in achromatopsia: an imaging study using spectral-domain optical coherence tomography. *Invest Ophthalmol Vis Sci*. 2010;51:5952–5957.
54. McCulloch DL, Marmor MF, Brigell MG, et al. ISCEV Standard for full-field clinical electroretinography (2015 update). *Doc Ophthalmol*. 2015;130:1–12.
55. Bach M, Brigell MG, Hawlina M, et al. ISCEV standard for clinical pattern electroretinography (PERG): 2012 update. *Doc Ophthalmol*. 2013;126:1–7.
56. Audo I, Michaelides M, Robson AG, et al. Phenotypic variation in enhanced S-cone syndrome. *Invest Ophthalmol Vis Sci*. 2008;49:2082–2093.
57. Bensinger E, Rinella N, Saud A, et al. Loss of foveal cone structure precedes loss of visual acuity in patients with rod-cone degeneration. *Invest Ophthalmol Vis Sci*. 2019;60:3187–3196.
58. Foote KG, De la Huerta I, Gustafson K, et al. Cone spacing correlates with retinal thickness and microperimetry in patients with inherited retinal degenerations. *Invest Ophthalmol Vis Sci*. 2019;60:1234–1243.
59. Tuten WS, Tiruveedhula P, Roorda A. Adaptive optics scanning laser ophthalmoscope-based microperimetry. *Optom Vis Sci*. 2012;89:563–574.
60. Bruce KS, Harmening WM, Langston BR, et al. Normal perceptual sensitivity arising from weakly reflective cone photoreceptors. *Invest Ophthalmol Vis Sci*. 2015;56:4431–4438.
61. Wang Q, Tuten WS, Lujan BJ, et al. Adaptive optics microperimetry and OCT images show preserved function and recovery of cone visibility in macular telangiectasia type 2 retinal lesions. *Invest Ophthalmol Vis Sci*. 2015;56:778–786.

Investigative Ophthalmology & Visual Science